SAND2024-01258J

Manuscript Title:

The Effects of Silicon and Niobium Concentration on the Solidification Behavior and Microstructure of Cast Monel Alloys

C. J. Farnin, E. N. Coker, P. A. Salinas, and J. N. DuPont

Corresponding Author- Christopher Farnin: Lehigh University, 5 E Packer Ave, Bethlehem PA, 18015, USA, cjf219@lehigh.edu, (267) 614-7090

Eric Coker: Sandia National Laboratories, P.O. Box 5800, Albuquerque, NM 87185, USA, encoker@sandia.gov

Perla Salinas: Sandia National Laboratories, P.O. Box 5800, Albuquerque, NM 87185, USA, pasalin@sandia.gov

John DuPont: Lehigh University, 5 E Packer Ave, Bethlehem PA, 18015, USA, jnd1@lehigh.edu

Abstract

Cast Monel alloys are used in applications requiring a combination of good mechanical properties and excellent resistance to corrosion. Despite prevalent industrial use, relatively few studies have been conducted to investigate the relationships between composition, solidification behavior, and microstructure. Given that these alloys are used in the cast and welded conditions, these factors have a significant influence over the material properties. In this work, microstructural characterization, electron probe microanalysis, x-ray diffraction, and differential scanning calorimetry were used to study how changes in Si and Nb concentrations affected the solidification path and microstructure of Monel alloys. It was found that increasing Nb concentration stabilized higher amounts of MC carbides and suppressed graphite formation during solidification. It was also found that the high nominal concentration and segregation of Si to the liquid led to the formation of $Ni_{31}Si_{12}$ and other silicides via terminal eutectic reactions at the end of solidification. A pseudo-binary solidification diagram was constructed using experimental data and was applied to predict the mass fraction of solidified eutectic as a function of composition. The modelled microstructures were found to be in good agreement with experimentally measured phase fractions.

1. Introduction

Monel alloys are used in a variety of applications that require a combination of good mechanical properties and excellent resistance to corrosion, including use in pipes, valves, and cladded coatings in marine environments [1–3]. These materials are commonly used in the cast and welded conditions, meaning that the properties are highly dependent on the nominal

composition, solidification behavior, and subsequent microstructure. The ASTM A494 specification defines the composition ranges of several different cast grades which span a variety of different Si and Nb concentrations [4]. Despite relative widespread use, few published works have systematically investigated how variations in composition affect the solidification path and microstructure of the alloys.

Several studies have characterized the as-solidified microstructure of low-Si (< 1 wt.%) Monel alloys and have shown that they predominantly solidify as single phase austenite [5–7]. As Si content is increased to 3 wt.% and higher, Si-rich eutectic constituents were reported to form in the interdendritic regions, however questions still remain as to the identity of these phases and how they form [8–10]. X-ray diffraction studies by Evgenov *et al.* and Wang *et al*. identified silicides such as β_1-Ni_3Si, $Ni_{31}Si_{12}$, and possibly δ-Ni_2Si in the solidified microstructure of similar Ni-Cu-Si alloys, but stopped short of characterizing the general solidification behavior or reaction sequences [8,9]. The cause of the eutectic reactions has been attributed to the partitioning of Si to the liquid during solidification, however no published works have performed quantitative characterization to describe the segregation behavior [8]. Solid state precipitation of Ni-Si phases have also been identified in the cast microstructure of medium and high-Si grades [8,9]. The most prevalent of these phases is widely regarded to be β_1, which has an $L1_2$ structure, akin to the γ'-Ni_3Al phase used to strengthen traditional Ni-base superalloys [9,11–13]. Despite its detection within the microstructure of some Monel alloys, the conditions necessary to induce the β_1 precipitation reaction are not well understood [9,11].

Changes in Nb concentration and the Nb to C ratio have also been documented to alter the solidification path and microstructure of Monel alloys, but have been subject to limited prior

research [10,14]. Eash and Kilhgren, and Sahoo *et al.* both showed that graphite formed in the cast microstructure of alloys containing very low Nb contents and at least ~0.17 wt.% C [10,14]. As Nb concentration was increased, NbC formed due to its strong affinity for carbon. The presence of MC carbides in the microstructure of other Monel alloys has been reported when sufficient concentrations of Nb or Ti were present [5,15].

Several of these studies have documented that the mechanical properties were highly sensitive to changes in composition [8,10,14]. Sahoo *et al.* reported that yield and tensile strength both increased significantly at higher Si and Nb concentrations, but that ductility was subsequently reduced [14]. These trends have been confirmed by several other reports and are also reflected in the minimum tensile requirements listed in the ASTM A494 specification [4,8,10]. Despite the documented changes to properties, no published works have performed sufficient characterization to quantitatively explain how changes in composition altered the solidified microstructures. Similarly, no computational or experiment-based solidification models have been presented or validated in literature to predict solidification path and microstructure. The objective of this work was to investigate the fundamental relationships between the composition, solidification behavior, and microstructure in cast Monel alloys, and to develop a predictive model to describe how microstructure changes as a function of composition. Given the established influence of composition on properties, this work will serve as a foundation to help engineer desirable microstructures and optimize performance in these materials.

2. Material and Methods

Table 1 shows the compositions of the alloys investigated in this work which contained variations in Si and Nb concentrations that spanned the ranges listed in the ASTM A494 specification. Both elements were varied systematically at low, medium, and high levels so that the individual and coupled effects could be readily distinguished. The alloys were fabricated by melting virgin elements in an alumina crucible, heating to a peak temperature of 1550 ºC, and then pouring into a 6" x 15" x 2" graphite mold under an Ar atmosphere. Prior to pouring the melt into the 2" x 6" face, a zirconia coating was applied to the interior of the mold. No mold preheat was utilized. Chemical analysis was performed on each casting in accordance with ASTM E1097-12 and E1019-18 [16,17].

Table 1. Nominal compositions of the cast Monel alloys used in this study. All values shown in wt.%.

Alloy	Description	Ni	Cu	Fe	Si	Nb	Mn	C	Al
1	High Si, Low Nb	Fill	30.29	3.38	4.41	0.50	1.48	0.31	0.04
2	Med Si, Low Nb	Fill	30.33	3.57	2.98	0.51	1.52	0.33	0.03
3	Low Si, Low Nb	Fill	29.94	3.57	1.08	0.51	1.53	0.32	0.03
4	Med Si, Med Nb	Fill	29.31	3.48	2.94	1.42	1.50	0.31	0.04
5	High Si, High Nb	Fill	29.66	3.45	4.42	2.70	1.52	0.30	0.05
6	Low Si, High Nb	Fill	29.69	3.58	1.07	2.76	1.52	0.32	0.04
7	Med Si, High Nb	Fill	29.65	3.50	2.90	2.60	1.50	0.32	0.04

Samples for characterization were cut from areas near the center of each casting, mounted in conductive polymer, and metallographically prepared to a final polish of 0.05 μm. Some samples were etched by swabbing with a solution of 8 g $FeCl_3$, 25 mL HCl, and 100 mL water (ASTM Etchant No. 38) [18]. Microstructural characterization was performed using a Hitachi-4300 field emission scanning electron microscope (SEM) using secondary and backscattered electron (BSE) detectors. X-ray energy dispersive spectroscopy (EDS) was conducted using an EDAX detector and the Genesis software to qualitatively measure the chemistry of phases in the microstructure [19]. Quantitative image analysis was performed by collecting 15 images of the as-polished microstructure of each alloy and thresholding them using the ImageJ/FIJI software [20]. To determine the volume percent of total Ni-Si eutectic-type constituents within each alloy, 10 additional images were collected at higher magnifications, such that the lamellar structures filled the imaging window. Thresholding was then performed to determine the relative fractions of each phase within the constituents and were then paired with the previously measured phase volume percents to calculate the overall amount of eutectic via Equation 1.

$$f_e = \frac{f_{int}}{f^e_{int}} \quad [1]$$

Where f_e is the fraction eutectic, f_{int} is the volume fraction of intermetallic measured in the overall microstructure, and f^e_{int} was the volume fraction intermetallic within the eutectic constituents. While the term eutectic is used, it is acknowledged that they formed in a multicomponent system and thus not through a true binary eutectic reaction. The fine spacing of the lamellar structures and/or low contrast between phases within the constituents in Alloys 5 and 7 complicated the measurements, so the average phase fractions from the eutectics in the

other alloys (which were in close agreement to one another), were used in the calculations for those alloys.

Electron probe microanalysis (EPMA) was performed using a JXA-8900 SuperProbe with an accelerating voltage of 15 kV, beam current of 30 nA, and working distance of 11 mm. X-ray counts were converted to weight percent using the Probe for EPMA software, along with scans taken from pure element standards [21]. The compositions of secondary phases were evaluated through a minimum of eight focused-beam measurements. To measure the overall composition of eutectic constituents, analog-beam scans were performed using a magnification that allowed the beam to raster over the lamellar structure of the constituents. To characterize solute segregation within the austenitic matrix, 16 x 16 grids of focused-beam measurements were collected on samples from each casting with a point spacing of 200 μm. Solute concentration profiles were assembled for each element using the weighted interval rank sort (WIRS) scheme [22]. The fraction of primary phases that formed prior to austenite solidification (e.g. MC carbides) were ignored during fraction solid assignments. Solute partition coefficients (k) were calculated using the procedure from Ganesan *et al.* by replotting the WIRS-assembled concentration profiles in accordance with Equation 2, a rearrangement of the classic Scheil non-equilibrium equation, and applying a linear fit [22].

$$\ln(C_s) = (k-1)\ln(1-f_s) + \ln(kC_0) \quad [2]$$

where C_s is the concentration of solute in the solid, C_0 is the nominal concentration, and f_s is the fraction solid. The slope of the trendline was then used to compute k for each element. The use of this Scheil-type analysis assumes that the alloys solidified under non-equilibrium conditions where there was negligible diffusion in the solid phase, infinite diffusion in the liquid phase,

equilibrium at the solid-liquid interface, and no dendrite tip undercooling. The average concentration of solute elements measured in the EPMA grids had close agreement with the reported nominal concentrations of each alloy indicating negligible macrosegregation had occurred over the areas selected for characterization.

X-ray diffraction was conducted on samples cut from each alloy over a 2θ interval of 20-110º and with a step size of 0.013º to aid in phase identification. To avoid texturing effects induced by the oriented grain structures, samples were ground into a powder using a 65 HRC metal file. Differential scanning calorimetry (DSC) was performed to measure the phase transition temperatures during melting and solidification using a Netzsch STA 449F3 Jupiter Thermal Analyzer. Sample masses of 180 mg were cut from each casting adjacent to the areas removed for microstructural characterization and were tested in an Ar atmosphere using a constant ramp rate of 10 ºC/min (0.167 ºC/s). Samples were placed in enclosed, high purity alumina crucibles, heated to peak temperatures of 1315 ºC or 1375 ºC (depending on the expected liquidus temperature), held for three minutes to ensure complete melting, and then cooled. Phase transformation temperatures were taken at the deviation from the local baseline. SEM imaging was performed on the DSC samples after testing to confirm that the solidification path and microstructure were representative of the castings.

Scheil solidification calculations were performed using TC-Python and the TCNi11 database to predict the effect of the composition on the solidification behavior and microstructure of the alloys [23–25]. The Ni-Si binary phase diagram was also constructed using Thermo-Calc and the TCBIN database for comparison with experimental measurements [26].

3. Results and Discussion

In the absence of experimental data in literature, solidification modeling using the calculation of phase diagrams (CALPHAD) approach has been used with great success to understand relationships between composition, solidification path, and microstructure [27–29]. Scheil solidification simulations were performed using Thermo-Calc by inputting compositions with systematic variations in Si and Nb concentrations. It was found that for many of the assessed alloys containing appreciable Si contents, Thermo-Calc was unable to properly complete the simulations. Calculated datapoints were frequently separated by significant fraction solid intervals resulting in large portions of the solidification simulation that were devoid of results because the required thermodynamic data were not available over much of the composition space. Because of the gaps and discontinuities in the calculations, the modelled solidification data were not deemed reliable. Modifications to existing thermodynamic CALPHAD databases may be necessary to properly describe the behavior of cast Monels. These issues reinforced the need for alternative methods of solidification modeling that utilize a phase diagram that is based on experimentally verified data.

3.1 Microstructural Characterization

The cast microstructures of the two 1 wt.% Si heats, containing low and high-Nb contents, are shown in Figure 1a and 1b respectively. The low-Nb alloy microstructure was comprised of an austenitic matrix with low fractions of high aspect ratio NbC particles and dark flakes. These flakes were identified as graphite via EDS scans which showed strong enrichment in C and a depletion in all other solute elements. The script morphology of the NbC and its

presence along the grain boundaries suggested it formed after primary austenite solidification through a eutectic reaction [30,31]. The reaction sequence of the graphite phase, which has previously been reported to form directly from the liquid or through eutectic reactions, was not clear [32,33]. Figure 1b shows the microstructure of the low-Si, high-Nb alloy which also exhibited an austenitic microstructure with groupings of mostly primary, faceted NbC particles. Carbides with this morphology are known to form directly from the melt and are often agglomerated into groups as they were pushed along by the solid/liquid interface during solidification, before becoming entrapped in the austenite [31]. The lack of graphite in this alloy suggested that all of the carbon reacted with Nb, a strong MC stabilizer, or went into solid solution within the matrix. The elevated Nb concentration also increased the NbC volume fraction, as is evident qualitatively by the NbC peak intensities in the XRD spectra in Figure 2, and measured phase fractions. The change in NbC morphology and place in the solidification path was most likely also the result of the higher Nb concentration and increase to carbide stability. While other factors such as solidification rate can play a role, both alloys were cast using identical procedures, and samples were removed from similar regions within the castings [31,34]. Higher magnification SEM imaging also revealed that both low-Si alloys exhibited isolated areas containing nanoscale precipitates. These areas were found exclusively around grain boundaries where EPMA measurements indicated Si concentration was locally elevated.

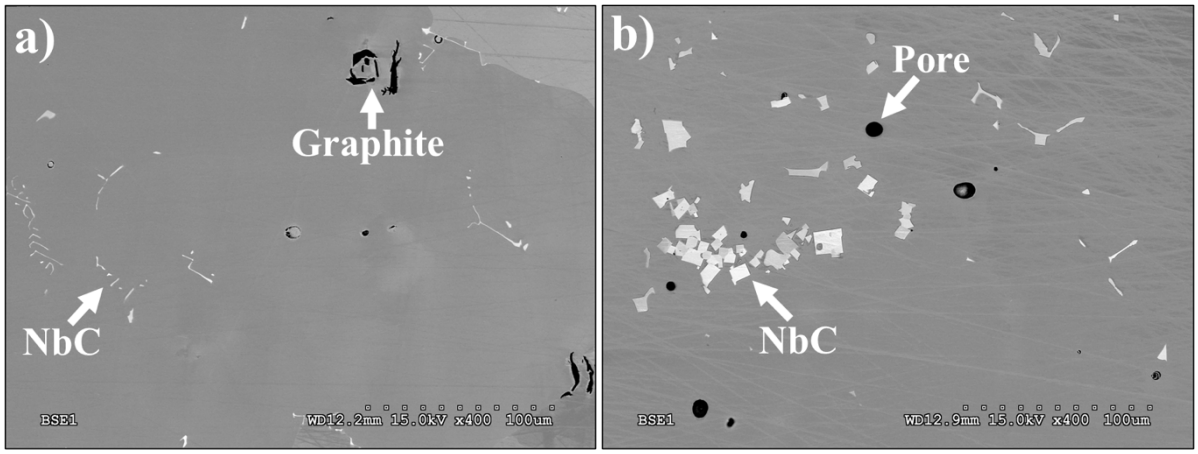

Figure 1. SEM-BSE images showing the microstructure of the low-Si Monel alloys in the as-cast condition for a) Alloy 3 containing 0.51 wt.% Nb, and b) Alloy 6 containing 2.76 wt.% Nb.

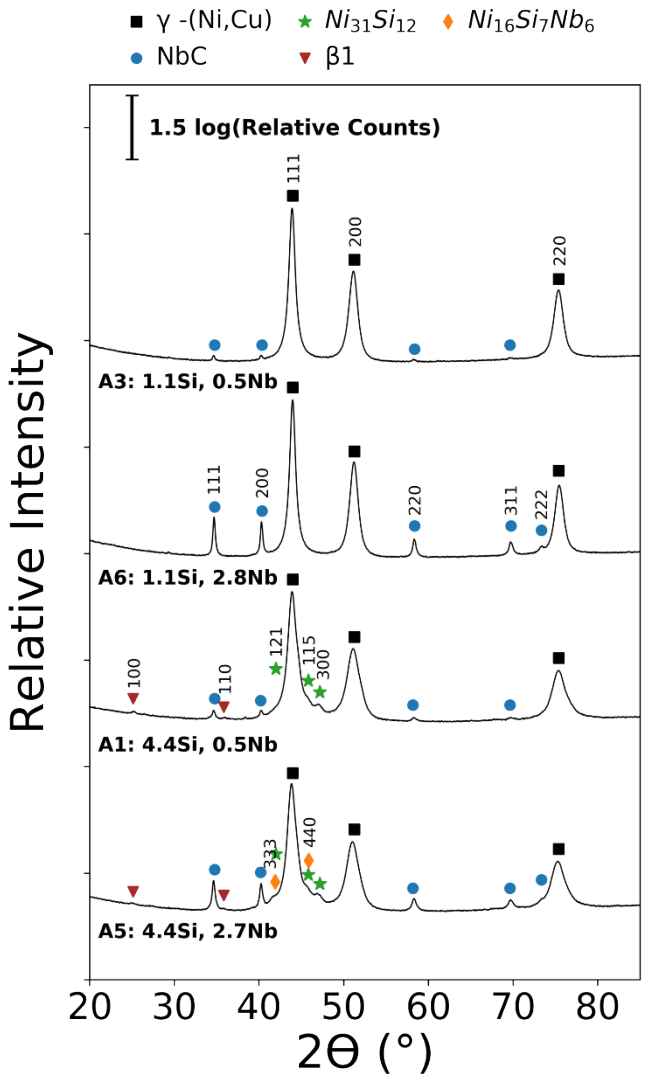

Figure 2. Powder x-ray diffraction patterns showing characteristic peaks for different phases identified in Alloys 3, 6, 1, and 5.

The microstructure of Alloy 4, which contained medium Si and Nb concentrations of 3 wt.% and 1.4 wt.% respectively, is shown in Figure 3. The intermediate Nb concentration resulted in the formation of primary, faceted carbides, similar to those observed in Alloy 6, however very small quantities of graphite were also present. In the interdendritic regions, two distinct intermetallic phases were identified within eutectic constituents. The total measured

amount of γ/intermetallic eutectic within the microstructure was 0.6 vol.% and thus was below the detection limit of the XRD scans. EPMA composition measurements conducted on these phases are recorded in Table 2 and show that the phases had differing Si concentrations. The higher-Si phase had a measured concentration close to that expected for $Ni_{31}Si_{12}$ (27.91 at.% Si). By assuming that Cu, Mn, Fe, and Nb substituted for Ni, the stoichiometry of the measured phase was estimated and is also shown in the table. The lower-Si intermetallic was found in very small amounts in Alloys 2 and 4, and had a measured Si concentration consistent with β_1 [35]. The stoichiometry was estimated based on the site-specific solubility study conducted by Tianxiang *et al*. and was in close agreement with the expected values for β_1 [13]. Both $Ni_{31}Si_{12}$ and β_1 have been previously reported to form in similar alloys in literature [8,9,36,37].

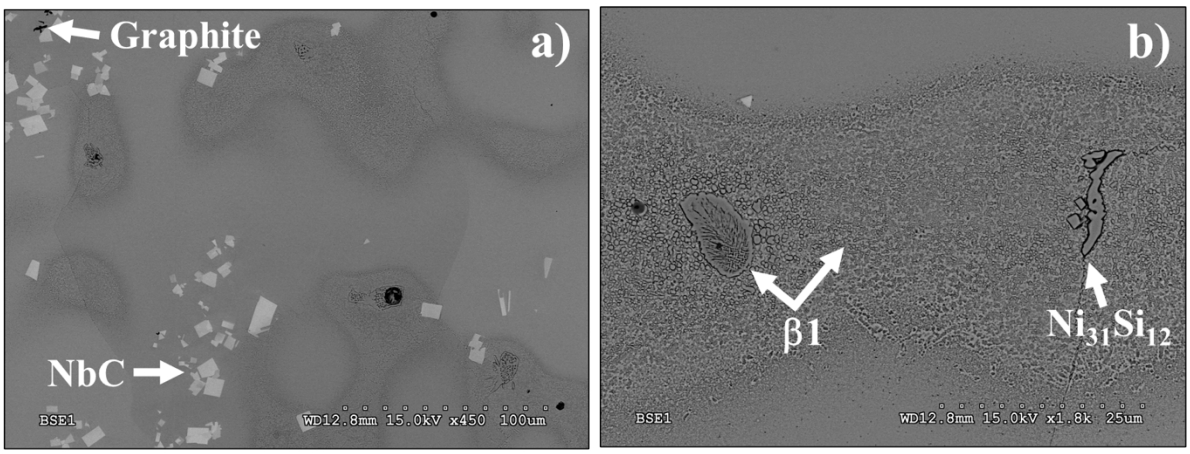

Figure 3. Representative SEM-BSE images showing the microstructure of Alloy 4 (3 wt.% Si, ~1.4 wt.% Nb) at a) low magnification, and b) higher magnification.

Table 2. Average compositions of eight EPMA measurements collected from intermetallic phases found in the Monel alloys. All values are shown in at.%. and errors represent the standard deviations between average compositions from each alloy.

Phase	Ni	Cu	Si	Fe	Mn	Nb	Measured Stoichiometry	Measured Alloys
$Ni_{31}Si_{12}$	68.51 ±0.26	2.45 ±0.30	27.93 ±0.17	0.62 ±0.10	0.46 ±0.05	0.02 ±0.02	$A_{31.0}B_{12.0}$ A= (Ni, Cu, Fe, Mn, Nb) B= Si	1, 2, 4,5
Ni_3Si (β)	69.47 ±0.31	6.30 ±0.34	22.18 ±0.09	1.04 ±0.12	0.98 ±0.01	0.02 ±0.01	$A_{3.1}B_{1.0}$ A= (Ni, Cu, Fe) B= (Si, Fe, Mn, Nb)	2, 4
$Ni_{16}Si_7Nb_6$ (G Phase)	57.33	2.58	24.59	0.99	2.64	11.86	$A_{16.6}B_{7.1}C_{5.2}$ A= Ni, B= Si C= (Nb, Mn, Cu, Fe)	5

Figure 3b shows that the interdendritic regions in Alloy 4, and the other 3 wt.% Si alloys, had a granulated appearance due to the presence of micro/nanoscale precipitates, presumably β_1 based on prior literature [9,11]. A distinct gradient in the size, shape, and distribution of precipitates was observed between the interdendritic and dendrite core regions. This is more clearly shown in the higher magnification image in Figure 4. Around the intermetallic eutectic constituents, the precipitates were relatively large and had irregular shapes. Moving towards the dendrite core, the precipitate size decreased, and the particle morphologies gradually transitioned to cubic and then spherical. Differences in precipitate morphology have been well documented in other alloys strengthened with $L1_2$ phases, and is generally attributed to changes in the lattice misfit between the precipitate and surrounding matrix [38,39]. Variations in the misfit strain may have resulted from variations in β_1 particle size, or from shifts in the austenite lattice parameter induced by solute concentration gradients between the interdendritic and dendrite core regions.

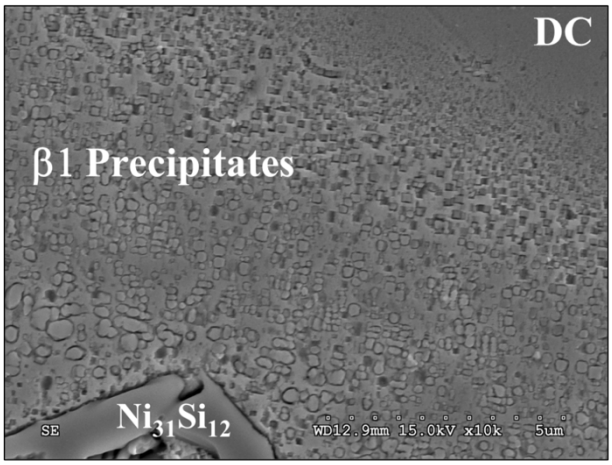

Figure 4. SEM image showing the differences in β_1-Ni_3Si size and morphology between the interdendritic region and dendrite core (DC).

The other 3 wt.% Si variants had similar microstructures to Alloy 4 despite the differences in Nb concentrations. Alloy 2 contained the same intermetallic phases, but also contained secondary NbC and graphite phases which were both present with script morphologies. Alloy 7 was found to have similar Ni-Si intermetallic constituents, but they were present with a much finer lamellar spacing that prevented direct EPMA measurements to confirm the phase identities. The higher Nb concentration in this heat also resulted in a high fraction of primary NbC particles, and the elimination of graphite from the microstructure.

Figure 5 shows the microstructures of the high-Si alloys containing 4.4 wt.% Si. The microstructure of the high-Si, low-Nb heat in Figure 5a contains secondary graphite colonies, similar to Alloy 2, but primary NbC particles which is at odds with the other low-Nb alloys. Intermetallic eutectic constituents were also present in high fractions in the interdendritic regions. EPMA measurements showed that these phases also had concentrations consistent with $Ni_{31}Si_{12}$. A large fraction of precipitates was observed in nearly all regions of the microstructure. The XRD results for this alloy in Figure 2 show representative peaks for $Ni_{31}Si_{12}$ which, when paired with the measured stoichiometries in Table 2, provided strong evidence to confirm the identity of the prolific intermetallic eutectic constituent in the medium and high-Si alloys. As prior work has acknowledged, several similar silicide phases in the Ni-Si system such as Ni_2Si, exhibit similar reflections to $Ni_{31}Si_{12}$ during XRD testing, and can not be ruled out from having formed during solidification or cooling [8]. The XRD patterns also show low-intensity peaks consistent with the β_1 phase in both high-Si grades. With the identity of the eutectic constituent already accounted for, these peaks confirm that the precipitate phase in the medium and high-Si alloys was β_1.

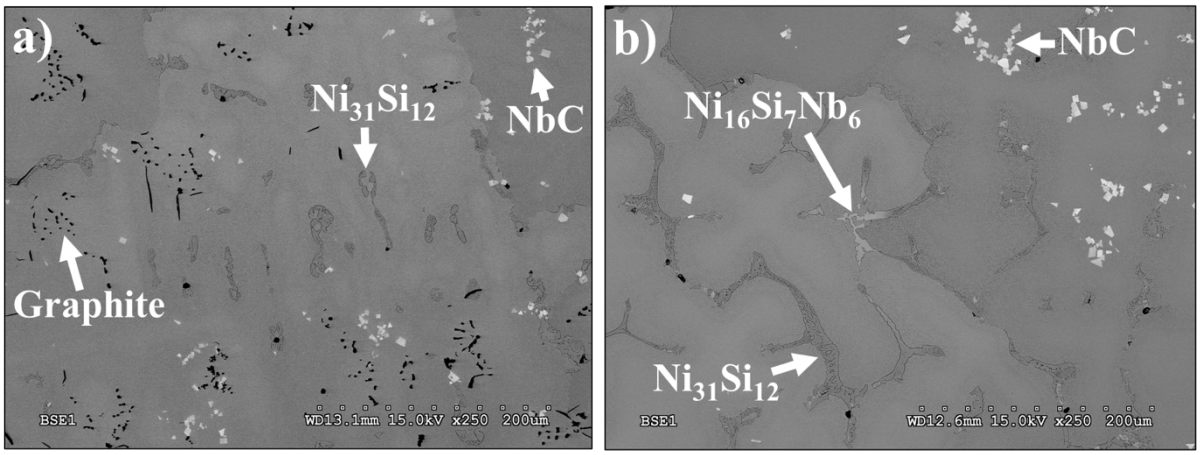

Figure 5. SEM-BSE images displaying the effect of Nb on the microstructures of the high-Si (4.4 wt.% Si) Monel alloys showing a) Alloy 1 containing 0.5 wt.% Nb, and b) Alloy 5 containing ~2.7 wt.% Nb.

The microstructure of the high-Si, high-Nb heat is shown in Figure 5b and is similar to that of Alloy 1, but with an additional Ni-Si-Nb intermetallic phase present. EPMA measurements in Table 2, and representative peaks in the XRD scan, suggest that this constituent is G phase ($Ni_{16}Si_7Nb_6$), which has been shown to form in other Ni-base alloys containing sufficient Nb and Si [40,41]. The stoichiometry of the phase was estimated using EPMA data and guidance from the work of King *et al*, who modelled the substitution energies of solute elements on the different atomic sites within G phase in steels [42]. The measured values showed good agreement with the expected stoichiometry.

The quantitative relationships between composition and phase fractions are summarized in Figure 6. The nominal Si concentration was shown to have a strong correlation with the measured fraction of Ni-Si eutectic constituents across the three Si levels. The eutectic fraction was not significantly altered by Nb concentration, although the fraction eutectic in Alloy 5 was increased compared to the lower-Nb variant. The general insensitivity to Nb content showed that

Si is the controlling element in intermetallic eutectic formation. Alternatively, as Nb concentration was raised, the fraction NbC increased significantly, while the amount of graphite was reduced and suppressed entirely at the highest-Nb level.

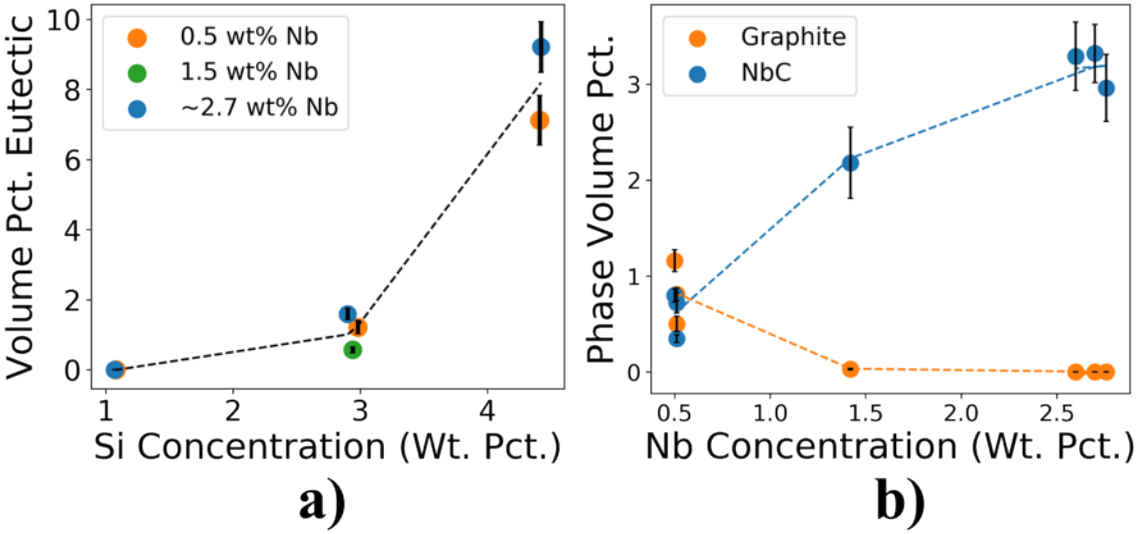

Figure 6. a) The influence of Si and Nb concentration on the volume percent of the intermetallic eutectic constituents, and b) the effect of Nb concentration on the volume percent graphite and NbC. Error bars show the standard error from image analysis measurements.

In addition to the obvious effects of Nb on the formation of graphite and NbC, more complex interactions with Si concentration were also observed. Despite having little to no solubility in either phase, the measured volume fractions of graphite and NbC, plotted in Figure 7, showed a clear positive correlation with Si concentration despite fixed Nb and C contents. The change in NbC fraction was accompanied by the previously mentioned transition in carbide reaction sequence, where secondary carbides were observed in the low and medium-Si heats (Alloys 3 and 2), while primary NbC was solely present in the high-Si heat. Although prior work has reported that Si may interact with C to promote graphite formation, or alter the

thermodynamic activity and/or solubility of C in steels, the relationships between Si concentration and the formation of C-enriched phases have not been well studied in Ni-base alloys [43,44].

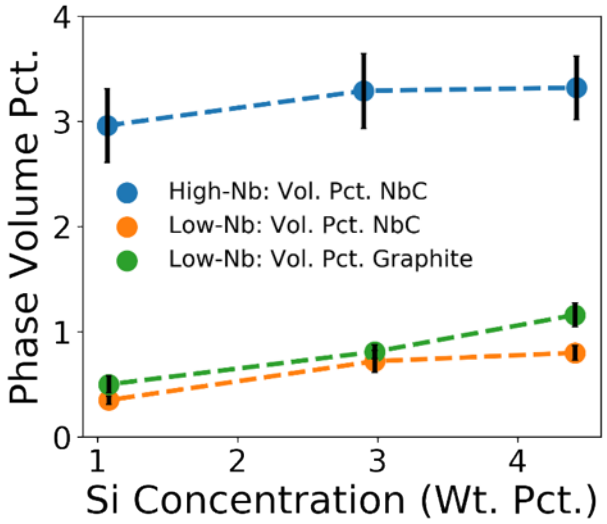

Figure 7. The influence of Si conc. on the volume percent of NbC and Graphite in low and high-Nb Monels. Error bars show the standard error of the measurements.

3.2 Solidification Path and Phase Transition Temperatures

DSC testing was performed to gain insight into how composition affected the sequence and temperatures of phase transformations during solidification. Table 3 lists the transformation temperatures measured in each alloy, and Figure 8a shows example DSC cooling curves for the three low-Nb Monel alloys. All transformation temperatures were taken from the on-cooling (OC) data, except for the liquidus temperature (T_L), which was taken at the peak of austenite melting on-heating (OH) as shown in Figure 8b. The on-heating T_L was not subject to undercooling effects and was more representative of the conditions during fusion welding where solidification occurs epitaxially from preexisting base metal grains.

Table 3. Phase transformation temperatures measured via DSC for each Monel alloy.

Alloy	Description	L→ L + γ OH (°C)	L→ L + γ + NbC OC (°C)	L→ L + γ + Graphite OC (°C)	L→ γ + $Ni_{31}Si_{12}$ OC (°C)	β_1 Solvus Temperature OC (°C)
1	High Si, Low Nb	1214	-	1175	1050	897
2	Med. Si, Low Nb	1252	1226	1194	1043	-
3	Low Si, Low Nb	1310	-	-	-	-
4	Med. Si, Med. Nb	1265	-	-	-	-
5	High Si, High Nb	1224	-	-	1055	897
6	Low Si, High Nb	1309	-	-	-	-
7	Med Si, High Nb	1260	-	-	-	-

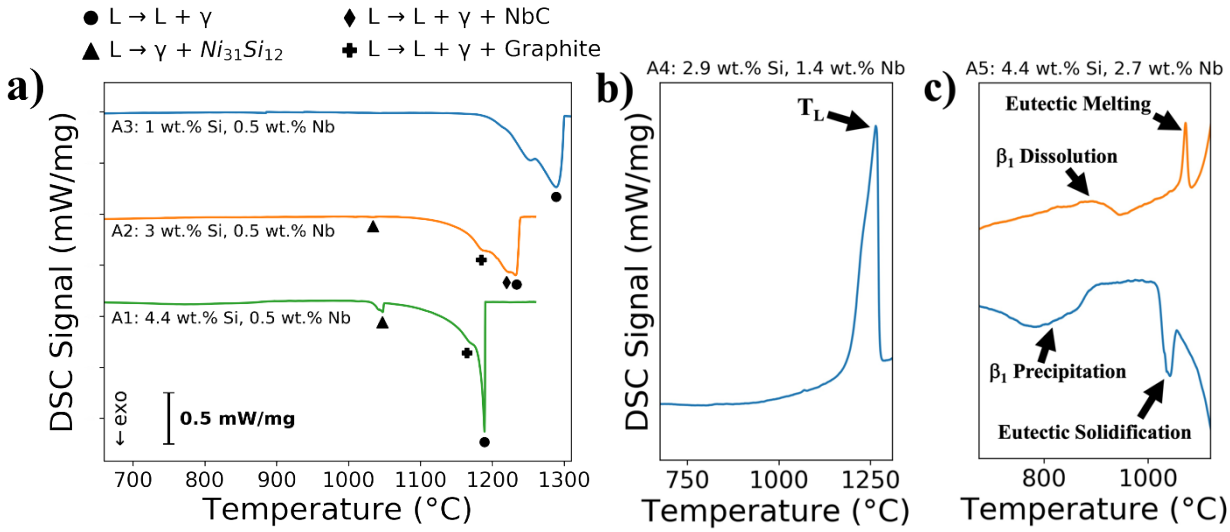

Figure 8. a) On-cooling DSC data for Alloys 3, 2, and 1 with exotherms marked with indicators. b) On-heating DSC data for Alloy 4 demonstrating the liquidus temperature measurement procedure. c) Zoomed in regions of Alloy 5 heating (upper) and cooling (lower) curves showing endo/exotherms for the solid-state dissolution/precipitation of β_1. The on-cooling data have been shifted vertically by 0.15 mW/mg for clarity.

A linear relationship was found between the T_L and the nominal Si concentration, as it dropped by ~93 ºC as Si content increased from 1-4.4 wt.%. This change was more significant than the melting point depression effects of Si in the Ni-Si binary system, where the same change in resulted in a 53 ºC decrease in T_L. Small exothermic peaks were visible ~1050 ºC in the cooling data of several medium and high-Si alloys. The peak areas correlated with the measured eutectic volume fractions and were thus attributed to the $\gamma/Ni_{31}Si_{12}$ eutectic reactions. These exotherms were not detected in Alloys 4 and 7 due to the low eutectic fractions and associated heat released.

Changes in the Nb concentration did not have a discernable effect on T_L. EPMA measurements performed on the solidified alloys (discussed in the next section) indicated that

most of the Nb in the Monel castings resides within the NbC phase. Unlike the low-Nb heats, the medium and high-Nb alloys formed predominately primary NbC which solidified at temperatures greater than T_L (i.e., prior to the start of austenite solidification) and resulted in a depletion of Nb in the surrounding liquid. Greater fractions of primary NbC at higher nominal Nb concentrations led to more substantial Nb depletion in the liquid accordingly. At the onset of austenite solidification (T_L), the discrepancy in remaining Nb concentration in the liquid between the low, medium, and high-Nb grades was thus minimal and did not significantly alter T_L. The reaction temperatures for primary NbC solidification were not detected in the DSC measurements, but several alloys exhibited small peaks or inflection points immediately below T_L corresponding to the formation of secondary carbides and/or graphite. Examples are clearly shown for each of the low-Nb heats in Figure 8a. While only a single peak below T_L was resolvable in the DSC curve for Alloy 3, both graphite and secondary NbC were found in the solidified microstructure, meaning that the specific transformation producing the exotherm could not be determined. The cooling curve for Alloy 2 showed two exotherms near the austenite solidification peak which was consistent with the presence of secondary NbC and graphite that were present with script morphologies in the cast microstructure. Given the expected solidification path of Ni-base alloys, the first peak was attributed to the γ/NbC reaction which depleted the liquid of MC stabilizing elements, and the second peak was thus attributed to the γ/graphite eutectic-type reaction at lower temperatures. While the microstructure of Alloy 1 also contained graphite and NbC, the carbide morphology indicated that it formed prior to austenite solidification, and suggested that the single thermal event between T_L and the eutectic temperature (T_e) must have been a result of the γ/graphite reaction.

Figure 8c displays portions of the heating and cooling curves from Alloy 5, and shows two broad endo/exotherms above the background which were consistent with the solid-state dissolution/precipitation of β_1. Other thermal analysis studies have also shown that the precipitation of $L1_2$ phases like γ' can occur over broad temperature ranges, comparable to the observations in Figure 8c [45,46]. The β_1 solvus temperature was taken at the onset of the β_1 exotherm on-cooling, and was measured to be 897 ºC in both high-Si alloys. An early study by Lashko *et al.* claimed that β_1 precipitation occurred in high-Si Monels within the temperature interval of 1000-700 ºC during air cooling which is consistent with the measured solvus temperature [11].

3.3 Solute Segregation Behavior

Prior works have shown that the solidification behavior and secondary phase formation in Ni-base alloys under low to moderate cooling rates typical of casting and welding are well described by the non-equilibrium solidification model which assumes negligible diffusion in the solid phase, infinite diffusion in the liquid phase, equilibrium at the solid/liquid interface, and no dendrite tip undercooling [39,47,48]. To characterize how solute segregation incurred during non-equilibrium solidification may have influenced the microstructure of cast Monel alloys, solid concentration profiles were generated using sorted EPMA data. Solute partition coefficients were calculated from the data to quantify the extent of segregation for each element and are listed in Table 4. The value of k is defined as the ratio between the concentration of solute in the solid (C_s) and liquid (C_L) phases at a fixed temperature and has traditionally been used in conjunction

with the Scheil equation to describe the evolution of C_s or C_L as a function of fraction solid (f_s) through Equations 3 and 4 [49].

$$C_s = kC_0\,(1 - f_s)^{k-1} \quad [3]$$

$$C_L = C_0\,(1 - f_s)^{k-1} \quad [4]$$

Table 4. Solute partition coefficients for different elements measured in each cast Monel alloy compared to other values reported in literature.

Alloy	k Ni	k Cu	k Fe	k Mn	k Si	k Nb
1	1.01	0.99	1.20	0.78	0.83	-
2	1.02	0.97	1.19	0.79	0.79	-
3	1.03	0.93	1.11	0.89	0.89	1.30
4	1.03	0.94	1.23	0.80	0.79	-
5	1.03	0.95	1.29	0.74	0.82	0.96
6	1.05	0.90	1.14	0.87	0.90	1.20
7	1.03	0.95	1.25	0.80	0.79	1.02
Monel 400 [7]	1.08	0.78	-	-	-	-
Nb-Bearing Superalloys [47]	1.02	-	1.00	-	0.76	0.45
HR-160 [50]	0.96	-	-	-	0.71	-
Incoloy 909 [51]	0.97	-	1.10	-	0.67	0.49

Example solute profiles for Alloy 4 (medium-Si, medium-Nb) are shown in Figure 9. Ni and Fe are both shown to segregate to the solid phase/dendrite core and have k values greater than unity. Elements Cu, Mn, and Si are shown to partition to the liquid phase/interdendritic regions and thus have k values less than unity. The partition coefficients for Ni, Fe, and Si were in close agreement with other values reported in literature, while Cu was measured to segregate less than was previously reported in a study on welded Monel 400 [7]. Solid concentration curves calculated using Equation 3 and the measured k values for each element were also plotted in black in Figure 9 for comparison. The partition coefficients for Ni, Cu, Fe, Mn, and Si were shown to be highly consistent between alloys and reflect that variations in Si and Nb concentration do not significantly affect the segregation behavior of those elements in the Monel system.

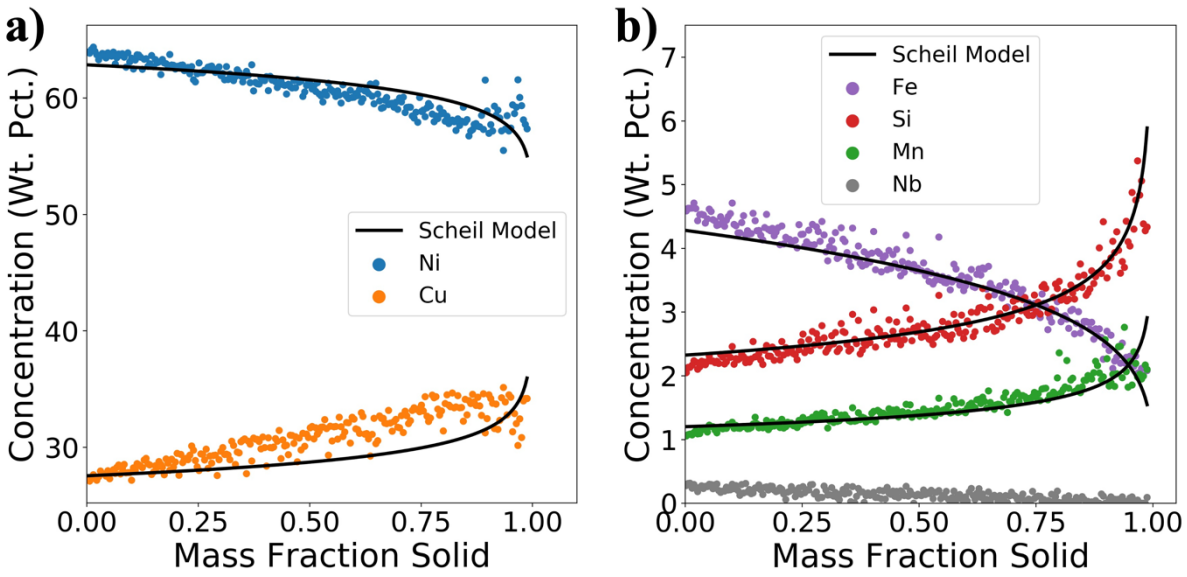

Figure 9. Representative solute profiles measured from Alloy 4 showing how a) Ni and Cu, and b) Fe, Si, Mn, and Nb segregate within the austenitic matrix. Black curves represent the predicted concentration profiles from the Scheil model using the calculated partition coefficients.

Table 4 shows k^{Nb} listed for several of the alloys, however the low matrix concentration and high degree of scatter in the measurements prevented accurate calculations for Alloys 1, 2, and 4. Niobium was generally found to segregate to the dendrite core in most of the alloys which was markedly different than the behavior previously reported in literature for other Ni-base alloys [47,51,52]. Previous works have shown that Nb typically segregates strongly to the liquid, with k values between 0.44-0.49 in alloys such as Incoloy 909 and Inconel 718 [47,51,52]. Among the three high-Nb heats, k^{Nb} was found to decrease significantly as a function of nominal Si concentration, varying from 1.20-0.96. This marked a change in the Nb segregation behavior as it transitioned from strongly segregating to the dendrite core, to very weak partitioning to the interdendritic region. The lower partition coefficient and higher liquid concentration of Nb near the end of solidification in Alloy 5 was consistent with the formation of G phase in that alloy.

To further investigate the findings that Nb segregated to the dendrite core during solidification in most of the castings, Thermo-Calc Scheil simulations were performed using the TCNi11 database for a series of example alloy compositions (based on the composition of Alloy 6) with Cu concentrations varying from 10 to 30 wt.% [25]. Copper was suspected to influence Nb segregation in the Monel system, as Nb is known to have extremely limited solid solubility in FCC-Cu, and also segregates to the dendrite core ($k > 1$) in the Cu-Nb binary system [53]. The C concentration in the simulated alloys was set to zero, as most C was expected to solidify as primary NbC, and the Nb concentration was selected to match the amount expected to remain in the liquid at the onset of austenite solidification (i.e. the average matrix concentration of 0.9 wt.% measured in Alloy 6). Silicon was omitted from the modelled system to avoid the previously discussed simulations errors. The results of the modelling are presented in Figure 10

and show the Nb concentrations in austenite as a function of fraction solid. The data for the 30 wt.% Cu alloy shows that Nb segregated strongly to the dendrite core during solidification in agreement with the k^{Nb} value of 1.20 measured in Alloy 6 and the observed behavior in Figure 9b. The predicted concentration profiles in the lower-Cu variants confirmed that Nb partitioning in the Monel system was heavily influenced by the nominal concentration and segregation behavior of Cu. When the nominal Cu concentration in the simulated alloys was reduced to 10 wt.%, Nb initially segregated to the liquid at low f_s values, which was consistent with the higher Ni concentration and expected behavior from literature, but transitioned back to solid enrichment as solidification progressed. This was attributed to the simultaneous segregation of Cu to the liquid, which locally altered the chemical environments of the solid and liquid phases as Cu accumulated at high f_s values.

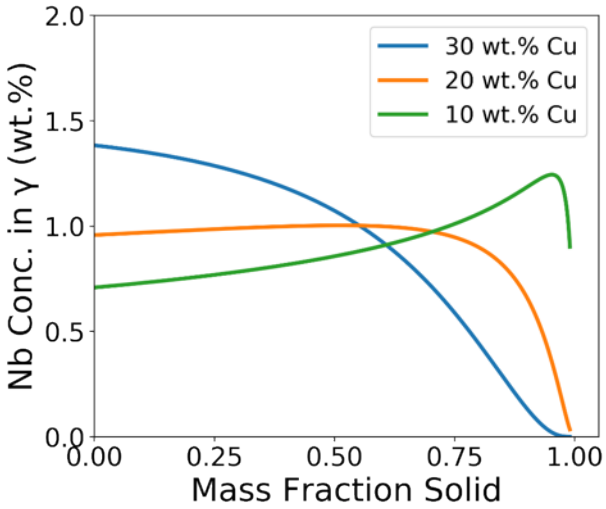

Figure 10. Results of Thermo-Calc Scheil simulations showing differences in the predicted Nb solid concentration profile in a Ni- X wt.% Cu- 3.5 wt.% Fe- 1.5 wt.% Mn- 0.9 wt.% Nb Monel alloy with varying Cu concentration.

Figure 9b also shows that the matrix concentration of Nb was significantly lower than the nominal concentration of 1.4 wt.%. As Si concentration was raised, the amount of Nb dissolved in the matrix decreased and a larger proportion was allotted to NbC. This effect can likely be attributed to the previously discussed correlation between increasing Si concentration and NbC volume fraction shown in Figure 7. The solidification of NbC prior to, or immediately after, the onset of austenite solidification reduced the amount of Nb within the liquid, leaving less solute available to go into solution in the austenite upon further cooling. Niobium is a highly effective solid solution strengthener in Ni-base alloys, and thus the decrease in the matrix concentration would be expected to impair the mechanical properties of the castings [54,55].

The segregation of Si in the Monel system is also of particular interest due to the formation of the Si-rich eutectic constituents at the end of solidification. The solid concentration profiles of Si in each alloy are plotted together in Figure 11. The large range of Si concentrations across the dendrites in the 3 wt.% Si alloys helps explain the gradient in β_1 precipitation that was observed during microstructural characterization. Areas in the interdendritic regions with higher Si concentrations would have a higher degree of supersaturation in the matrix, and thus increased driving force for precipitation when the austenite solubility limit was reduced at lower temperatures during cooling. The 4.4 wt.% Si heats had higher Si concentrations near the dendrite core, which was consistent with the more even dispersion of precipitates found in those microstructures. The concentration profiles for both the medium and high-Si alloys approached the same maximum Si concentration at the end of austenite solidification, indicating that the solubility limit had been reached. The average maximum solid solubility limit of Si in the matrix of the eutectic-bearing alloys was 4.99 ± 0.21 wt.%. This was measured by empirically fitting the

concentration data to polynomials, which closely matched the segregated profiles while being insensitive to noise in the EPMA data, and using the equations to determine the interdendritic concentrations at high-f_s values. Figure 11 appears to show that several measurements had higher Si concentrations than the measured solubility limit. This was due to the presence of large, coarsened precipitates in the interdendritic regions that formed during cooling from the supersaturated matrix and created localized Si-enriched and Si-depleted regions that were sampled during EPMA data collection. The actual Si solid solubility limit in austenite was thus approximated via curve-fitting through the scattered data rather than simply taking the maximum Si concentration which would have been artificially inflated. In the higher-Si alloys, the solubility limit was reached earlier on in the solidification process (lower f_s values) than in the medium-Si heats, resulting in larger fractions of $\gamma/Ni_{31}Si_{12}$ eutectic constituents that formed from the remaining solute enriched liquid. The polynomial equations were also used to measure the dendrite core concentrations (for $f_s = 0$) in each alloy and had excellent agreement with the experimentally measured Si concentration profiles at low-f_s values.

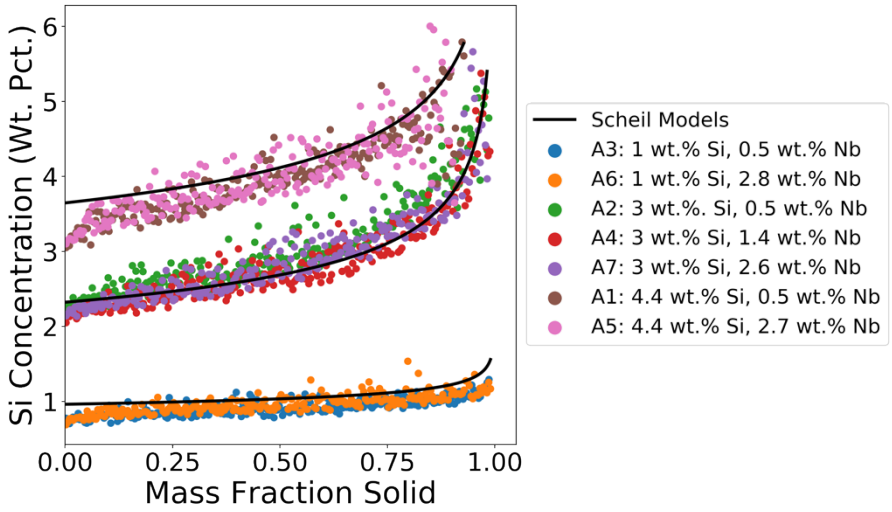

Figure 11. Silicon concentration profiles measured in each of the Monel alloys. Black curves represent the predicted concentration profiles from the Scheil model using the calculated partition coefficients.

The segregation profiles of the 1 wt.% Si alloys maintain relatively low concentrations, even in the interdendritic regions. Given the low nominal concentration, the non-equilibrium solidification model predicts that the Si concentration was not expected to approach the solubility limit until $f_s >> 0.99$. Any appreciable segregation in the low-Si heats would thus occur over very small regions along grain boundaries that were either under sampled by the EPMA measurements or were subject to electron beam interaction volume effects that resulted in lower measured concentrations.

3.4 Construction of Pseudo-Binary Solidification Diagram

Quantitative models that improve the understanding of composition- microstructure relationships, and that can make predictions about the solidification behavior of new alloy

compositions are essential. Particularly for cases where traditional CALPHAD models were ineffective, pseudo-binary eutectic solidification diagrams have been used successfully to model the solidification path and microstructure of Ni-base alloys [56–59]. While diagrams of this type may have the appearance of binary phase diagrams, the term solidification diagram is used because the data utilized in the diagram construction are not necessarily in true thermodynamic equilibrium. For a system to be effectively modelled as pseudo-binary, several key assumptions must be valid. The formation of the eutectic constituent must be dependent on the nominal concentration and segregation behavior of the dependent element. Also, the amount of each phase within the eutectic constituent, the eutectic composition, and the eutectic reaction temperature must remain relatively constant as a function of the dependent element concentration, just as in a true binary system.

The cast Monel system meets these requirements and can be well approximated as a pseudo-binary eutectic system, where the Ni-Cu-Fe-Mn-Nb-C solid solution austenitic matrix acts as the solvent, and Si acts as the solute. The formation of $\gamma/Ni_{31}Si_{12}$ was shown to result from the segregation of Si to the liquid during solidification, and the fraction eutectic was shown to be predominantly controlled by the nominal Si concentration. The eutectic Si concentration (C_e) was measured to be 10.61 ± 0.35 wt.% via analog EPMA scans on each eutectic-bearing alloy (except Alloy 7 where the constituents were deemed too small to reliably collect measurements). The measured C_e within the Monel alloys was in agreement with the eutectic concentration of 11.45 wt.% in the Ni-Si binary system. The low standard deviation between the measurements in different alloys reflected the consistency of both the C_e and ratio of phases within the

constituents. The eutectic reaction temperatures listed in Table 3 were also measured to be in close agreement with one another and indicated minimal dependence on composition.

With the pseudo-binary condition established, the solidification diagram was assembled and is presented in Figure 12. The eutectic point was plotted in black at the center of the diagram in accordance with the EPMA measured C_e and the average measured T_e. While small quantities of eutectic β_1 and G phase were found in several heats, the amounts of these phases were negligible compared to the fraction of $Ni_{31}Si_{12}$ and were thus ignored in the creation of the diagram. The liquidus line was created using the nominal Si concentrations of the alloys as the x-coordinates and DSC measured liquidus temperatures as the y-coordinates. A linear fit was applied to these data, along with the eutectic point, and had excellent agreement with the measured values. The equation of the liquidus line describing T_L as a function of Si concentration in weight percent (C^{Si}) is given by Equation 5.

$$T_L = -27.33\, C^{Si} + 1339.3, \qquad r^2 > 0.99 \qquad [5]$$

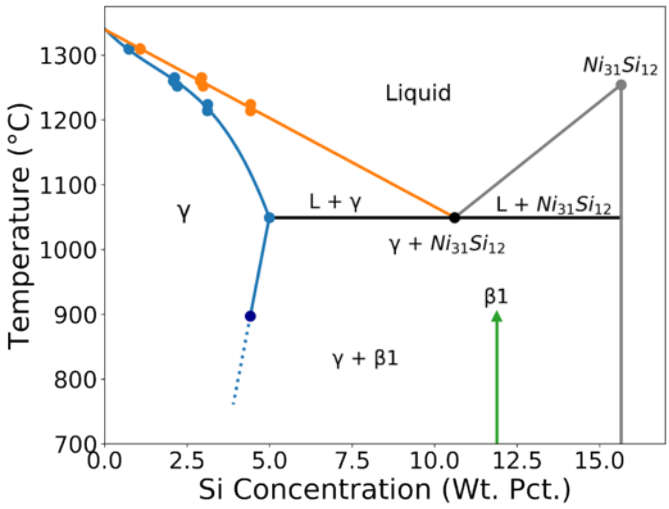

Figure 12. Proposed psuedo-binary solidification diagram for the cast Monel alloy system created using DSC, EPMA, quantitative image analysis, and data from literature.

The solidus curve was constructed by applying an empirical polynomial fit to a series of relevant solid concentration datapoints. The first solidus point was set as the y-intercept of the liquidus line (Equation 5), since both curves should converge to the same temperature for a 'pure' material without Si. Further points corresponding to the average Si content in the dendrite cores in each alloy were also plotted at the respective liquidus temperatures, representative of C_s in the first increment of solid to form upon cooling. The final point on the solidus line was plotted at the eutectic temperature and at the measured maximum solid solubility limit of Si in austenite (4.99 wt.%). The maximum solid solubility limit of Si in the Ni-Si binary system is 8.94 wt.%, indicating that the addition of the other alloying elements within the Monel system significantly reduced Si solubility within the matrix. The third order polynomial equation describing the solidus temperature (T_s) as a function of C^{Si} is given by Equation 6.

$$T_s = -2.88\,(C^{Si})^3 + 13.26\,(C^{Si})^2 - 52.76\,C^{Si} + 1340.68, \qquad r^2 > 0.99 \qquad [6]$$

$Ni_{31}Si_{12}$ was added to the diagram as a line compound in accordance with the fixed Si concentration of 15.65 wt.% measured via EPMA, and the lack of solid solubility reflected in the traditional Ni-Si binary phase diagram [35]. The corresponding hypereutectic liquidus line was approximated by applying a linear fit from the $Ni_{31}Si_{12}$ melting point, taken from the work of Du and Schuster, to the measured eutectic point [60]. A line for the β_1 phase was drawn at the Si concentration measured from the eutectic β_1 phase in Alloys 2 and 4, and was extended up to the solvus temperature measured in the high-Si grades. The $\gamma/\ \beta_1$ solvus line was estimated by drawing a line from the maximum solid solubility point to the β_1 solvus temperature measured in the 4.4 wt.% Si alloys (see Table 3) to model how the solubility of Si in austenite decreases as a function of temperature. While the solvus line offers an estimate of the onset temperatures of precipitation during cooling from casting, it does not represent a true equilibrium solvus line.

The structure of the diagram beneath the eutectic temperature was complicated by the unique condition in which the $Ni_{31}Si_{12}$ phase that formed in the eutectic reaction was distinct from the β_1 phase that precipitated out in the solid-state during further cooling. Due to the lack of experimental data, the phase boundary lines between the estimated solvus line and the $Ni_{31}Si_{12}$ phase boundary line from 897 to 1049 ºC were omitted. The actual phase boundary lines in this undefined region may be similar to those proposed by Li *et al,* who used CALPHAD modeling to create a metastable Ni-Si phase diagram in which the $L \rightarrow \gamma + \beta_3$ reaction was suppressed in place of the $\gamma + Ni_{31}Si_{12}$ reaction which better matched experimental observations in highly

undercooled binary melts [61]. That diagram contained an 18 ºC interval below the eutectic temperature where $\gamma + Ni_{31}Si_{12}$ was stable, before transitioning to $\gamma + \beta_2$, and then finally to $\gamma + \beta_1$ at lower temperatures [61]. Similar to the metastable diagram, solid-state transformations to other silicide phases found in the Ni-Si binary system, such as β_2 or β_3, may also be present beneath the eutectic line in the Monel system. Further testing on alloys with higher Si concentrations near C_e would be necessary to complete these regions of the diagram.

3.5 Validation of Proposed Solidification Diagram

To demonstrate the predictive capabilities of the proposed solidification diagram, Scheil-type calculations were performed to model the fraction eutectic expected to form as a function of varying nominal Si concentration (C_0). Note that the analytical forms of the classic Scheil equation (Equations 3 and 4) were derived under the assumption of a constant partition coefficient, which does not accurately reflect the varying k^{Si} represented in Figure 12 in which the liquidus line is linear and the solidus line exhibits substantial curvature. Thus, the differential mass balance form of the Scheil equation, given below as Equation 7, was used to conduct the calculations to account for the varying k^{Si}.

$$df_s = \frac{1 - f_s}{C_L - C_s} dC_L \quad [7]$$

Using the solidus polynomial equation to compute temperature as a function of C_s, an iterative calculation was performed by increasing C_s over small increments to generate a decreasing solidus temperature profile. These temperatures were then used to calculate the corresponding C_L at each increment using a rearrangement of the liquidus line equation (T_L (C^{Si}) converted to C^{Si} (T_L)). By taking dC_L as the difference between successive C_L increments, df_s could be determined through Equation 7 so long as the calculation was initiated at the start of solidification where f_s=0 and $C_L = C_0$. By iterating the procedure, f_s was continually updated by adding the df_s increments from the previous step. This procedure was used to determine C_L as a function of f_s for a series of example alloys with varying C_0. Since C_e was known, the differential Scheil calculation was used to compute f_s and thus the corresponding fraction liquid (f_L) remaining in the system when the eutectic point was reached ($C_L = C_e$). The remaining fraction liquid would solidify through the terminal $L \rightarrow \gamma + Ni_{31}Si_{12}$ eutectic reaction and was thus equal to the predicted mass fraction eutectic.

The results of the solidification diagram/differential Scheil analysis are shown in Figure 13 alongside the experimentally measured fraction eutectic measurements. The measured eutectic volume fractions were converted to mass fraction by assuming the density of the matrix and eutectic austenite to be 8.80 g/cm^3 and the density of the $Ni_{31}Si_{12}$ phase to be 7.82 g/cm^3 [3,62,63]. The eutectic fraction predicted using Equation 4 and the average k^{Si} value of 0.83 from Table 4, where f_L was also calculated for $C_L = C_e$, is plotted for comparison. These data show that the solidification diagram can be used effectively to predict eutectic formation in the cast Monel alloy system, as the calculated values are in good agreement with the experimentally measured fractions. The solidification diagram procedure significantly outperformed the

predictions from Equation 4 that used the fixed k^{Si}, as that procedure substantially underestimated the extent of Si segregation and subsequent eutectic formation.

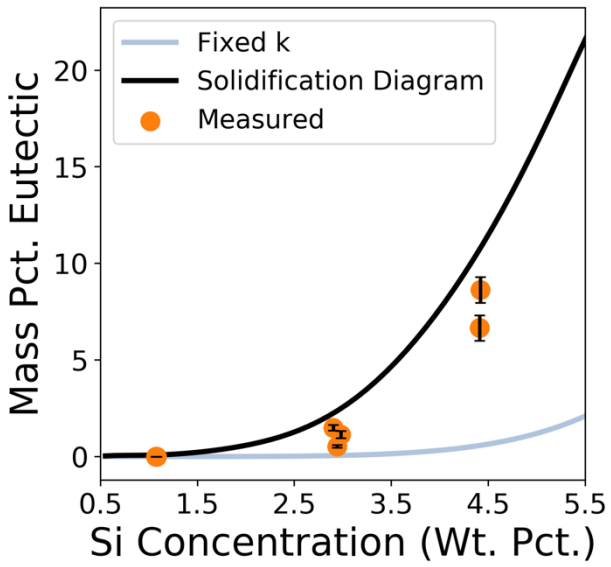

Figure 13. Predicted mass percent eutectic calculated using the solidus and liquidus data from the pseudo-binary solidification diagram. Measured values and predictions from the traditional Scheil equation with a fixed k=0.83 are plotted for comparison.

The differences between the solidification diagram predictions and measured values could have arisen from several possible sources of error. Deviations from the assumptions inherent to the pseudo-binary approximation, and/or changes to the actual solidus/liquidus contours beyond the empirical polynomial fits could produce error in fraction eutectic calculations. An underestimation of the maximum solid solubility limit of Si in austenite caused by electron beam interaction volume effects, or from improperly accounting for the scatter within the EPMA data, could also have resulted in an overestimation in the fraction eutectic. Another potential source of error was the use of the Scheil analysis which assumed complete non-equilibrium solidification conditions and thus no solid-state diffusion. Back diffusion incurred

during the solidification process can reduce the severity of solute segregation and result in reduced eutectic formation compared to non-equilibrium conditions. Calculation of the dimensionless diffusion parameter (α) was performed to evaluate if back diffusion played a role in the solidification of the Monel alloy castings, and to better understand the processing conditions over which the solidification diagram would be valid. The value of α is given by Equation 8, and can be used to approximate the extent of solid-state diffusion during solidification [64,65].

$$\alpha = \frac{D_s t_f}{L^2} \quad [8]$$

where D_s is the diffusivity of solute in the solid phase, t_f is the solidification time, and L is the diffusion distance (half the secondary dendrite arm spacing). For the condition where $\alpha \ll 1$, solid state diffusion is insignificant, and the solidification path is well estimated by the non-equilibrium model. As the value of α increases, solute has time to diffuse across a significant portion of the dendrite arm, and solidification deviates significantly from the non-equilibrium model.

The value of α was calculated as a function of cooling rate and is plotted in Figure 14. The solidification time was calculated as a function of the varied cooling rate using the DSC measured solidification temperature range ($T_L - T_e$) from Alloy 2, which exhibited the widest solidification interval among the alloys assessed in this work. The solid-state diffusivity of Si in pure Ni was taken from the work of Wang *et al.* at the solidus and liquidus temperatures of Alloy 2 and was used to compute two α curves that represented the upper and lower bound of solute

diffusivity experienced during the solidification process [66]. The diffusion distance/dendrite arm spacing was also set as a function of cooling rate using data from Bäckerud and Liljenvall in their study of a 89 wt.% Cu- 10 wt.% Ni- 1 wt.% Fe alloy [67]. The two α plots in Figure 14 show that solid-state diffusion of Si is generally small (α < 0.1) for cooling rates greater than 0.16 ºC/s, indicating that the solidification diagram should remain valid for those cooling conditions.

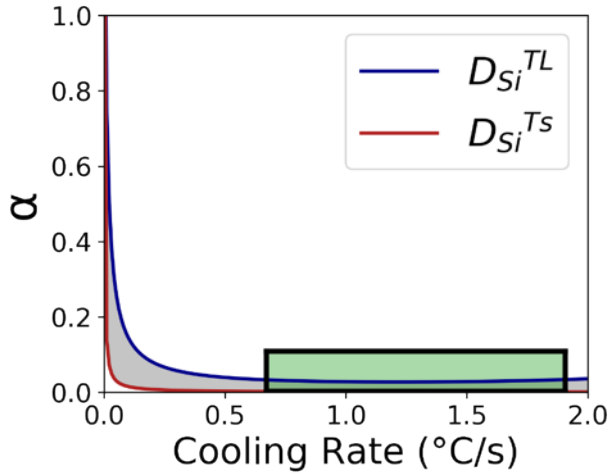

Figure 14. Dimensionless diffusion parameter (α) calculated as a function of cooling rate using diffusivity values at the liquidus and solidus temperatures. The range of MAGMASOFT modelled cooling rates for the Monel castings are shaded in green.

To determine if back diffusion was significant in the cast Monel alloys, a MAGMASOFT simulation was performed to model the cooling rates experienced by the castings during solidification [68]. The model was set up to reflect the actual casting conditions of the alloys by defining a graphite mold with proper interior dimensions, a two inch mold wall thickness, and 1550 ºC pour temperature. The thermal properties of the melt and solidifying alloy were taken from the Monel 400 alloy within the MAGMASOFT database. The chemistry of this alloy did

not contain Si, Nb, or C, but was still expected to provide the best possible estimation of the properties of the castings. Virtual thermocouples were placed at different locations midway through the thickness of the casting to track the cooling rates. The model predicted that the average cooling rate during solidification varied from 0.67-1.91 ºC/s depending on location, which was significantly higher than the 0.16 ºC/s limit where back diffusion was expected to become significant. The interval of modelled cooling rates was highlighted in green on the plots of α in Figure 14 and show that while some small amount of back diffusion may occur, the overall effect on the solidification behavior and subsequent microstructure of the cast Monel alloys should be negligible.

4. Conclusions

In this study, the effects of composition on the segregation behavior, solidification path, and microstructure of ASTM A494 cast Monel alloys were characterized and used to describe the solidification behavior of the alloy system. The following conclusions can be drawn as a result of this work.

1. The high C concentration in the cast alloys resulted in graphite formation during solidification for alloys containing 1.4 wt.% Nb and lower. Higher Nb concentrations suppressed graphite formation by stabilizing higher fractions of NbC earlier on in the solidification sequence.
2. Increasing nominal Si concentration promoted the formation of primary NbC during casting and reduced the partition coefficient of Nb from 1.20-0.96.

3. Segregation of Si to the liquid led to the formation of Si-rich intermetallic phases, primarily $Ni_{31}Si_{12}$, via eutectic reactions at the end of solidification in alloys containing a nominal Si concentration of 2.9 wt.% and greater.
4. The cast Monel system is well approximated as an austenite (Ni ,Cu, Fe, Mn, Nb, C) - Si pseudo-binary system, and a solidification diagram describing $\gamma/Ni_{31}Si_{12}$ eutectic solidification and solid-state β_1 precipitation was presented.
5. The proposed solidification diagram was shown to be effective at predicting the fraction $\gamma/Ni_{31}Si_{12}$ eutectic as a function of nominal Si concentration.

5. Acknowledgements

The authors would like to thank Dr. Richard Hardin for his valuble contribution in performing the MAGMASOFT modelling work. Sandia National Laboratories is a multi-mission laboratory managed and operated by National Technology and Engineering Solutions of Sandia, LLC, a wholly owned subsidiary of Honeywell International, Inc., for the U.S. Department of Energy's National Nuclear Security Administration under contract DE-NA0003525.

6. Funding

This research is sponsored by the DLA-Troop Support, Philadelphia, PA and the Defense Logistics Agency Information Operations, J68, Research & Development, Ft. Belvoir, VA.

7. Data Availability

Data will be made available upon request.

8. Conflict of Interest

The authors declare that they have no conflicts of interest.

9. References

1 L.E. Shoemaker and G.D. Smith: *JOM*, 2006, pp. 22–6.

2 H. Vastenholt and T. Fukuda: *Proc. Asia Pacific Oil Gas Conf.*, 1993, pp. 221–8.

3 Specialmetals.com: *Monel Alloy 400 Datasheet*, 2005.

4 *ASTM A494*, ASTM International, 2019.

5 O.O. Marenych, D. Ding, Z. Pan, A.G. Kostryzhev, H. Li, and S. van Duin: *Addit. Manuf.*, 2018, vol. 24, pp. 30–6.

6 K. Devendranath Ramkumar, N. Arivazhagan, S. Narayanan, M. Narayanan, A. Mondody, and R. Kashyap: *Adv. Mater. Res.*, 2012, vol. 383–390, pp. 4693–6.

7 I.D. Choi, D.K. Matlock, D.L. Olson, and E. Procedures: *Scr. Metall.*, 1988, vol. 22, pp. 1563–8.

8 S. Wang, J. Jie, B. Dong, S. Liu, T. Wang, and T. Li: *Mater. Sci. Technol. (United Kingdom)*, 2020, vol. 36, pp. 1671–84.

9 A.G. Evgenov, G.I. Morozova, and V.I. Lukin: *Met. Sci. Heat Treat.*, 2006, vol. 48, pp. 364–7.

10 J.T. Eash and T.E. Kihlgren: *Trans. Amer. Foundrymen's Soc.*, 1949, pp. 535–45.

11 N.F. Lashko, K.P. Sorokina, and A.N. Gorbunov: *Termicheskaya Obrab. Met.*, 1966, pp. 485–7.

12 T. Shinozawa, H. Murayarlia, and H. Mori: *Trans. JIM*.

13 Z. Tianxiang, L. Yundong, Z. Zhi, and Z. Yaoxiao: *MRS Proc.*, 1990, vol. 213, pp. 137–42.

14 M. Sahoo, R.J. Lacroix, and P. Newcombe: *AFS Trans.*, 2002, pp. 239–51.

15 I. Raffeis, F. Adjei-Kyeremeh, U. Vroomen, E. Westhoff, S. Bremen, A. Hohoi, and A. Bührig-Polaczek: *Appl. Sci.*, DOI:10.3390/APP10103401.

16 *ASTM E1097-12*, Conshohocken, PA, 2017, pp. 1-8.

17 *ASTM E1019-18*, Conshohocken, PA, 2018, pp. 1-22.

18 *ASTM E407-07*, Conshohocken, PA, 2015, pp. 1-22.

19 *EDAX Genesis Spectrum Software*.

20 M.D. Abràmoff, P.J. Magalhães, and S.J. Ram: *Biophotonics Int.*, 2004, vol. 11, pp. 36–41.

21 J.J. Donovan, D. Kremser, J.H. Fournelle, and K. Goemann: *Probe for EPMA Software: Acquisition, Automation, and Analysis*, Probe Software Inc., 2012.

22 M. Ganesan, D. Dye, and P.D. Lee: *Metall. Mater. Trans. A Phys. Metall. Mater. Sci.*, 2005, vol. 36A, pp. 2191–204.

23 J.O. Andersson, T. Helander, L. Höglund, P.F. Shi, and B. Sundman: *Calphad*, 2002, vol. 26, pp. 273–312.

24 *TC-Python API Program. Guid. Accessed 2022.*

25 *Thermo-Calc TCNi11 Ni-Base Superalloys Database. Accessed Feb 2022.*

26 *Thermo-Calc TCBIN Bin. Solut. Database. Accessed Jan 2023.*

27 L. Gong, B. Chen, Z. Du, M. Zhang, R. Liu, and K. Liu: *J. Mater. Sci. Technol.*, 2018, vol. 34, pp. 541–50.

28 R.A. Wheeling and J.C. Lippold: *Mater. Charact.*, 2016, vol. 115, pp. 97–103.

29 W. Stockdale and J.N. DuPont: *Sci. Technol. Weld. Join.*, 2011, vol. 16, pp. 426–32.

30 J.N. DuPont, C. V. Robino, J.R. Michael, M.R. Nous, and A.R. Marder: *Metall. Mater. Trans. A Phys. Metall. Mater. Sci.*, 1998, vol. 29A, pp. 2785–96.

31 A.K. Bhambri, T.Z. Kattamis, and J.E. Morral: *Metall. Trans. B*, 1975, vol. 6, pp. 523–37.

32 K. Yamamoto, M. Hashimoto, N. Sasaguri, and Y. Matsubara: *Mater. Trans.*, 2009, vol. 50, pp. 2253–8.

33 M.C. Flemings: *Solidification Processing*, McGraw-Hill, 1974.

34 Z.-H. Yu, L. Liu, X.B. Zhao, W.G. Zhang, J. Zhang, and H.Z. Fu: *Trans. Nonferrous Met.*

Soc. China (English Ed., 2010, vol. 20, pp. 1835–40.

35 P. Nash and A. Nash: *Bull. Alloy Phase Diagrams*, 1987, vol. 8, pp. 6–14.

36 J. Zhang, Z. Lu, L. Jia, H. Xie, X. Wei, and S. Tao: *Mater. Res. Express*, DOI:10.1088/2053-1591/ac4407.

37 H. Xie, L. Jia, and Z. Lu: *Mater. Charact.*, 2009, vol. 60, pp. 114–8.

38 V. Biss and D.L. Sponseller: *Metall. Trans.*, 1973, vol. 4, pp. 1953–60.

39 J.N. DuPont, J.C. Lippold, and S.D. Kiser: *Welding Metallurgy and Weldability of Nickel-Base Alloys*, Wiley, Hoboken, New Jersey, 2009.

40 F. Zupanic, C. Nunes, G. Coelho, P. Cury, G. Lojen, and T. Boncina: *Trans. Nonferrous Met. Soc. China (English Ed.*, 2018, vol. 28, pp. 2226–35.

41 V.O. Dos Santos, H.M. Petrilli, C.G. Schön, and L.T.F. Eleno: *Calphad Comput. Coupling Phase Diagrams Thermochem.*, 2015, vol. 51, pp. 57–66.

42 D.J.M. King, M. Yang, T.M. Whiting, X. Liu, and M.R. Wenman: *Acta Mater.*, 2020, vol. 183, pp. 350–61.

43 R.P. Smith: *J. Am. Chem. Soc.*, 1948, vol. 70, pp. 2724–9.

44 C.F. Walton and T.J. Opar, eds.: *Iron Castings Handbook: Covering Data on Gray, Malleable, Ductile, White, Alloy, and Compacted Graphite Irons*, Iron Castings Society, 1981.

45 S.M. Seo, H.W. Jeong, Y.K. Ahn, D.W. Yun, J.H. Lee, and Y.S. Yoo: *Mater. Charact.*, 2014, vol. 89, pp. 43–55.

46 P.R.S. Azevedo e Silva, R. Baldan, C.A. Nunes, G.C. Coelho, and A.M. da S. Costa: *Mater. Charact.*, 2013, vol. 75, pp. 214–9.

47 J.N. Dupont, C. V. Robino, A.R. Marder, and M.R. Notis: *Metall. Mater. Trans. A Phys. Metall. Mater. Sci.*, 1998, vol. 29, pp. 2797–806.

48 K.L. Zeisler-Mashl and B.J. Pletka: *Superalloys 1992*, 1992, pp. 175–84.

49 E. Scheil: *Zeitschrift für Met.*, 1942, vol. 34, pp. 70–2.

50 J.N. DuPont, J.R. Michael, and B.D. Newbury: *Welding Metallurgy of Alloy HR-160 (No. SAND99-1355J)*, Albuquerque, NM and Livermore, CA, 1999.

51 M.J. Cieslak, T.J. Headley, G.A. Knorovsky, A.D. Romig, and T. Kollie: *Metall. Trans. A*, 1990, vol. 21, pp. 479–88.

52 J.N. Dupont: *Metall. Mater. Trans. A Phys. Metall. Mater. Sci.*, 1996, vol. 27A, pp. 3612–20.

53 M. Hamalainen, K. Jaaskelainen, R. Luoma, M. Nuotio, P. Taskinen, and O. Teppo: *Calphad*, 1990, vol. 14, pp. 125–37.

54 H.A. Roth, C.L. Davis, and R.C. Thomson: *Metall. Mater. Trans. A Phys. Metall. Mater. Sci.*, 1997, vol. 28, pp. 1329–35.

55 Y. Mishima, S. Ochiai, N. Hamao, and M. Yodogawa: *Trans. Japan Inst. Met.*, 1986, vol. 27, pp. 656–64.

56 J. Andersson, S. Raza, A. Eliasson, and K.B. Surreddi: *8th Int. Symp. Superalloy 718 Deriv. 2014*, 2014, pp. 181–92.

57 G.A. Knorovsky, M.J. Cieslak, T.J. Headley, A.D. Romig, and W.F. Hammetter: *Metall. Trans. A*, 1989, vol. 20A, pp. 2149–58.

58 D.F. Susan, C. V. Robino, M.J. Minicozzi, and J.N. DuPont: *Metall. Mater. Trans. A Phys. Metall. Mater. Sci.*, 2006, vol. 37A, pp. 2817–25.

59 Y. Shen, M. Wang, H. Xia, L. Zheng, N. Ta, Y. Meng, and F. Cui: *Adv. Eng. Mater.*, 2021, vol. 23, pp. 1–8.

60 Y. Du and J.C. Schuster: 1999, vol. 30, pp. 2409–18.

61 X. Li, B. Zhang, T. Wang, Z. Liu, and T. Yu: *J. Alloys Compd.*, 2016, vol. 672, pp. 578–81.

62 *Data retrieved from the Materials Project for Si12Ni31 from database version v2022.10.28.*, DOI:10.17188/1201478.

63 A. Jain, S.P. Ong, G. Hautier, W. Chen, W.D. Richards, S. Dacek, S. Cholia, D. Gunter, D. Skinner, G. Ceder, and K.A. Persson: *APL Mater.*, DOI:10.1063/1.4812323.

64 T.W. Clyne and W. Kurz: *Metall. Trans. A, Phys. Metall. Mater. Sci.*, 1981, vol. 12A, pp. 965–71.

65 H.D. Brody and M.C. Flemings: *TMS-AIME*, 1966, vol. 236, pp. 615–23.

66 S. Wang, D. Liu, Y. Du, L. Zhang, Q. Chen, and A. Engström: *Int. J. Mater. Res.*, 2013, vol. 104, pp. 721–35.

67 L. Bäckerud and L.M. Liljenvall: *Met. Technol.*, 1979, vol. 6, pp. 463–76.

68 *MAGMA Gießereitechnologie GmbH, Aachen Ger.*